Enhanced Multiferroic Properties of YFeO$_3$ by Doping with Bi^{3+}

Omar Rosales-González [1], **Félix Sánchez-De Jesús** [1], **Fernando Pedro-García** [1], **Claudia Alicia Cortés-Escobedo** [2], **Màrius Ramírez-Cardona** [1] and **Ana María Bolarín-Miró** [1,*]

[1] Área Académica de Ciencias de la Tierra y Materiales, Universidad Autónoma del Estado de Hidalgo Mineral de la Reforma, Hidalgo 42184, Mexico

[2] Instituto Politécnico Nacional, Centro de Investigación e Innovación Tecnológica, Ciudad de Mexico 02250, Mexico

* Correspondence: anabolarin@msn.com

check for updates

Abstract: Tthe present work studied the cationic substitution of Y^{3+} by Bi^{3+} on the crystal structure of orthorhombic YFeO$_3$ and its effect over magnetic, dielectric and electric properties of multiferroic yttrium orthoferrite. Stoichiometric mixtures of Y$_2$O$_3$, Fe$_2$O$_3$ and Bi$_2$O$_3$ were mixed and milled for 5 h using a ball to powder weight ratio of 10:1 by high-energy ball milling. The obtained powders were pressed at 1500 MPa and sintered at 700 °C for 2 h. The test samples were characterized at room temperature by X-ray diffraction (XRD), vibrating sample magnetometer (VSM), scanning electron microscope (SEM), energy dispersive X-ray spectroscopy (EDS) and impedance spectroscopy (IS). The X-ray diffraction patterns disclosed a maximum solubility of 30 % mol. of Bi^{3+} into the orthorhombic YFeO$_3$. For higher concentrations, a transformation from orthorhombic to garnet structure was produced, obtaining partially Y$_3$Fe$_5$O$_{12}$ phase. The substitution of Bi^{3+} in Y^{3+} sites promoted a distortion into the orthorhombic structure and modified Fe-O-Fe angles and octahedral tilt. In addition, it promoted a ferromagnetic (FM) order, which was attributed to both the crystal distortion and Dzyaloshinskii-Moriya interaction. For doped samples, an increase in real permittivity values was observed, and reduced with the increase of frequency. This in good agreement with the Maxwell-Wagner effect.

Keywords: YFeO$_3$; Bismuth doped YFeO$_3$; high-energy ball milling; ferromagnetic; dielectric; multiferroic

1. Introduction

Multiferroic materials are those that exhibit at least two of three ferroic orders: Ferroelectricity, ferromagnetism, and ferroelasticity [1]. Multiferroic that combines ferromagnetic and ferroelectric behaviors, also known as magnetoelectric multiferroic, is quite rare compared to other multiferroic materials., However, there has been considerable scientific interest for its potential applications in electronic systems, especially in storage devices for recording and reading information [2–4]. However, there are still many design challenges for multiferroics materials, highlighting that this behavior is exhibited only at low temperature [5]. Bismuth ferrite (BiFeO$_3$) is the first generation of multiferroic materials that combine in a single phase ferroelectric and antiferromagnetic behavior at room temperature [6,7]. Furthermore, it presents many issues due to the formation of secondary phases that provide a high leakage current [8,9]. The second generation of multiferroic materials is composed by perovskites with the general formula RFeO$_3$ where R = Y, Ho, Lu, Er or Sc. [10] YFeO$_3$ is a second-generation multiferroic material. This material crystallizes in two polymorphic forms:

(i) Orthorhombic perovskite-type structure; and (ii) hexagonal structure. The orthorhombic $YFeO_3$ or yttrium orthoferrite, having distorted the perovskite structure, crystallizes in the centrosymmetric space group *Pnma*, with lattice parameters a = 5.5946 Å, b = 7.6040 Å, and c = 5.2790 Å. The centrosymmetric nature of this material is responsible for ferroelectric and weak ferromagnetic behaviors at room temperature. It presents a magnetic transition at the Neel temperature of ~640 K [11,12]. Magnetic ordering is related to three types of magnetic interactions in atoms bonds: Y-Y, Y-Fe and Fe-Fe where Fe-O-Fe super-exchange interaction is the main source of the weak ferromagnetic behavior as well as the canting of magnetic moments of Fe^{3+} due to the Dzyaloshinskii-Moriya (DM) interaction [10,13]. Further, centrosymmetric structures are not ferroelectric in nature, however distortions in the structure can modify it [14]. For $YFeO_3$ materials, *Pnma* centrosymmetric structure induces polarization arising from canted antiferromagnetic ordering and structure distortion [15,16]. This indicates that multiferroic property of this material is associated with Fe-spins which induces electric polarization, partial substitution or doping with different ions in A or B sites (Y^{3+} and Fe^{3+} sites) which are an advantageous method to modify and sometimes enhance the multiferroic properties of $YFeO_3$ [17,18]. Many works have been focused on the doping of one of both atomic positions reporting interesting results in multiferroic properties. Jacobs et al. reported increased electrical conductivity with the partial substitution of Ca^{2+} for Y^{3+} into $YFeO_3$ crystal structure, which was attributed to the compensation of charge Ca^{2+} that produced a hole localization on Fe site [19]. The substitution on A-sites with magnetic ion Gd^{3+} enhanced the magnetic behavior mainly due to the new Gd-Gd, Gd-Fe interactions, structural distortions and microstrain induced in the $YFeO_3$ crystal structure [20,21]. Similar behavior was observed for the doping of Er^{3+} substituting Y^{3+} at low concentrations. Nevertheless, when Er^{3+} content increased, the weak ferromagnetic behavior was lost and acquired paramagnetic properties [22]. A dielectric properties study on $YFeO_3$, concerning to B site substitution of Fe^{3+} with Mn^{3+}, showed a reduction in relative permittivity and three dielectric relaxations in the function of temperature. Further, the results showed the important role of oxygen vacancies toward the dielectric relaxation process [3,17]. Madolappa et al. [11] reported an increased coercive field of $YFeO_3$ related with the use of Ti^{4+} as a doping ion. They demonstrated that the dielectric relaxation process corresponded to the non-Debye type. Additionally, Ti^{4+} promoted a long-range conductivity process. Regarding the above, R^{3+}-Fe interactions demonstrated an intimal relation with the magnetic and dielectric properties of the orthorhombic $YFeO_3$. Therefore, it is possible to modulate ferromagnetic and ferroelectric properties with the addition of rare earth cations with a different ionic size other than the Y^{3+} ionic ratio. It is expected that Bi^{3+} would enhance the ferroelectric behavior, in a similar way that occurs in $BiFeO_3$, but avoiding the formation of secondary phases and increasing the FeO_6 octahedron tilting, providing a ferromagnetic behavior.

This work reports a systematical study of the partial substitution of Y^{3+} by Bi^{3+} to modulate the ferromagnetic and dielectric properties of orthorhombic $YFeO_3$. The nature of the origin of ferromagnetic and dielectric properties has not been clearly explained yet, therefore it is important to evaluate individually the magnetic and the dielectric behaviors as indicators for its prospective application as multiferroic material.

2. Materials and Methods

Stoichiometric mixtures of precursor oxides: Iron oxide (Fe_2O_3, Sigma-Aldrich, St. Louis, MO, USA, 99.9% purity), yttrium oxide (Y_2O_3, Sigma-Aldrich, St. Louis, MO, USA, 99.9% purity) and bismuth oxide (Bi_2O_3, Sigma-Aldrich, St. Louis, MO, USA, 99.9% purity) were mixed following to Equation (1):

$$(1-x)Y_2O_3 + Fe_2O_3 + x\,Bi_2O_3 \rightarrow 2Y_{1-x}Bi_xFeO_3 \tag{1}$$
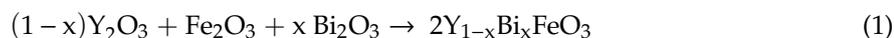
A total of 5 g of starting mixture was loaded along with steel balls of 1.27 cm of diameter in a cylindrical steel vial (50 cm^3) (steel/steel, S/S) at room temperature in an air atmosphere and milled for 5 h, using a shaker mixer mill (SPEX model 8000D, SPEX® SamplePrep, Metuchen, NJ, USA). The milled powders were uniaxially pressed into cylindrical test pieces at 1500 MPa. The test pieces were

annealed in an air atmosphere at 700 °C for 2 h. The structural characterization of all the products was made using an X-ray diffractometer Bruker D-8 (Bruker Corporation, Billerica, MA, USA) with Cu radiation (λ = 1.541874 Å) in the 2-theta range from 20 to 60 degrees. Refined lattice parameters, crystallite sizes, phase quantification (wt. %) and microstrain ($\mu\varepsilon$), were determined by Rietveld analysis using free-software, Material Analysis Using Diffraction (MAUD, Version 2.26, Trento, Italy)), for all synthesized samples. This method considers all the collected information in a diffraction pattern and uses a least-squares approach to refine the theoretical line profile until it matches the measured profile [23]. Starting crystallographic data were obtained from the Inorganic Crystal Structure Database (ICSD). The grain morphologies and porosity of sintered pellets were analyzed using a JEOL JSM-6300 scanning electron microscope (JEOL, Akishima, Tokio, Japan) working at an accelerating voltage of 15 kV. Energy-dispersive X-ray spectroscopy (EDS) microanalysis (EDAX, Mahwah, NJ, USA) was used to determine the elemental composition in SEM micrographs. Magnetization studies were carried out at room temperature using a vibrating sample magnetometer (VSM) model MicroSense EV7 (Microsense LLC, Lowell, MA, USA), with a maximum field of ±18 kOe. The Curie temperature was determined by means of a temperature scan test under a magnetic field of 10 kOe and it was taken as the intersection point with the temperature axis of the tangent to the magnetization curve with the most negative slope. Impedance spectroscopy was performed using a LCR meter Model HIOKI Hi-TESTER, 3532-50 (HIOKI, Nagano, Japan) at room temperature, in a frequency range from 10^2 to 5×10^6 Hz. Previously, both sides of test pieces were coated with an Au-Pt alloy through the sputter coating process.

3. Results and Discussions

3.1. Structural Characterization

Figure 1 shows the X-ray diffraction (XRD) patterns for different stoichiometric mixtures of Y_2O_3, Fe_2O_3 and Bi_2O_3, milled for 5 h, pressed at 1500 MPa and sintered at 700 °C for 2 h in order to obtain $Y_{1-x}Bi_xFeO_3$ test pieces (Δx = 0.1, $0 \leq x \leq 0.5$). As can be observed in Figure 1, the X-ray diffraction pattern belonging to the un-doped $Y_{1-x}Bi_xFeO_3$ sample (x = 0), the formation of orthorhombic $YFeO_3$ ($YFeO_3$, ICSD #80865, *Pnma*) can be confirmed by the presence of its diffraction peaks. After doping with low contents of bismuth (x $\leq$ 0.3), two gradual phenomena could be observed. The decreased peak diffraction broadened in relation with the increased amounts of Bi^{3+} concentration, and shifted toward to low angles of the diffraction peaks, as shown on the right of Figure 1. It is a consequence of Y^{3+} substitution by the Bi^{3+} into the yttrium orthoferrite crystal structure which increased their lattice parameters due to their larger size radii ion. By increasing the bismuth concentration (x $\geq$ 0.4), new diffraction peaks belonging to yttrium iron garnet (YIG, $Y_3Fe_5O_{12}$, ICSD #60167, *Ia3d*) appeared, and it was accompanied with sillenite ($Bi_{25}FeO_{40}$, ICSD #68627, *I-23*) as a secondary phase.
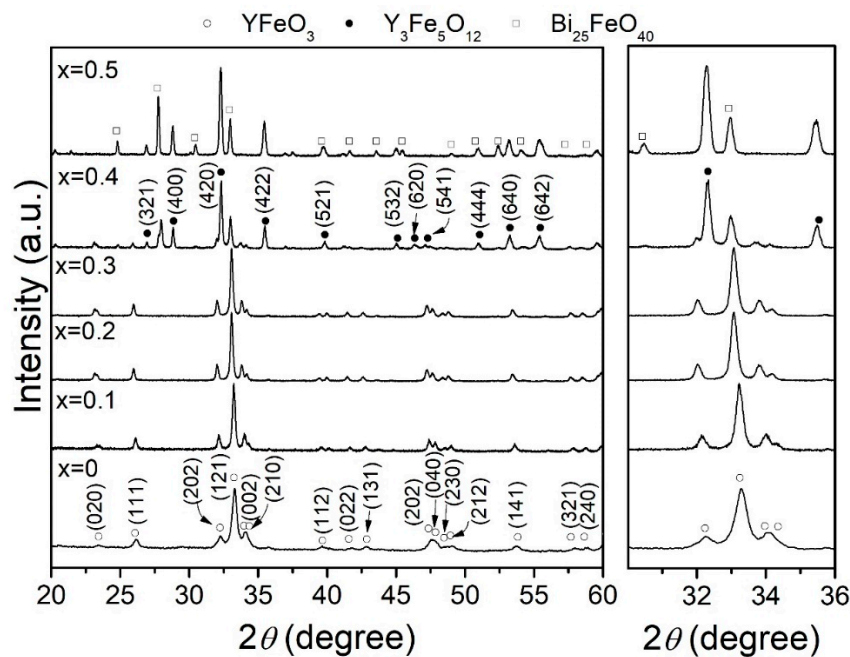
Figure 1. XRD patterns of samples of mixtures of Y_2O_3, Fe_2O_3 and Bi_2O_3 milled for 5 h and sintered at 700 °C for obtaining $Y_{1-x}Bi_xFeO_3$ ($0 \leq x \leq 0.5$, $\Delta x = 0.1$).

The phase transformation or decomposition of yttrium orthoferrite was completed for x = 0.5, and it was induced due to the $YFeO_3$ orthorhombic phase which was an intermetallic compound, with a stoichiometric composition. Therefore, it just introduced small amounts of dopants. In the studied compositions, a maximum amount of 0.3 mol. of bismuth can be introduced into the yttrium position of the orthorhombic crystal structure (solubility), in good agreement with Van Hook's phase diagram [24,25]. In general, it was observed that a decrement in broadening peak reflections with the increment of doped level (x), was associated with modifications in the crystallite size and microstrain.

Rietveld refinements were carried out to study the evolution of the cell parameters, crystallite size, microstrain, and phase quantification as the Bi^{3+} concentration (x) was increased. The results are presented in Table 1. Through phase quantification, it possibly confirmed that samples with low Bi^{3+} concentrations (x ≤ 0.3) were mainly composed of pure orthorhombic $YFeO_3$. However, when the bismuth was higher than 0.4, the amount of orthorhombic $YFeO_3$ decreased until 15.97 wt. %, with an increment of the yttrium iron garnet (YIG or $Y_3Fe_5O_{12}$) approximately 73.67 in wt. %, and 10.36 wt. % of $Bi_{25}FeO_{40}$. Moreover, for x = 0.5 sample, a complete phase transition to the garnet structure was confirmed, though $Bi_{25}FeO_{40}$ (13.32 wt. %) as a secondary phase was still present. In reference with refined parameters, it can be observed that the lattice parameters increased systematically, while the microstrain decreased as bismuth content increased. This can be attributed to the substitution of Y^{3+} with smaller ionic radii (0.90 Å) by a larger ionic radii cation Bi^{3+} (1.03 Å) [26]. Also, the microstrain can be correlated with the increased crystallite size and hence with the grain growth which promoted the liberation of internal stress of the crystal structure. These results explain the diminution of the broadening of peaks with the bismuth content, observed qualitatively in the XRD patterns shown in Figure 1. In the particular composition of x = 0.4, the polymorphic transition from orthorhombic $YFeO_3$ to garnet $Y_3Fe_5O_{12}$ produced a diminution in microstrain, independently to crystallite size. It was attributed to the preference of Bi^{3+} to form $Bi_{25}FeO_{40}$; rather than introduce into the crystal structure to obtain Bi doped $YFeO_3$. The refinement parameters exhibited a good adjustment, as the low values of R_{wp} and χ^2 have shown.

Table 1. Rietveld analysis of the XRD patterns to $Y_{1-x}Bi_xFeO_3$ pellets of all compositions.

Level Doped (x)	Phase Space Group	% Phase	Lattice Parameters (Å)			Crystallite Size (Å)	$\mu\varepsilon$ ($\times 10^{-4}$)	χ^2	R_{wp}
			a	b	c				
0	YFeO$_3$ *Pnma*	100 ± 0.7230	5.2683 ± 0.0005	5.5510 ± 0.0004	7.5764 ± 0.0005	911.11 ± 56.58	41.41 ± 0.0001	1.03	12.04
0.1	YFeO$_3$ *Pnma*	100 ± 0.6692	5.2714 ± 0.0004	5.5664 ± 0.0004	7.5845 ± 0.0005	929.39 ± 31.46	16.24 ± 0.0006	1.16	17.49
0.2	YFeO$_3$ *Pnma*	100 ± 0.5242	5.2974 ± 0.0002	5.5854 ± 0.0002	7.6224 ± 0.0003	1270.91 ± 31.25	11.77 ± 0.0001	1.20	16.34
0.3	YFeO$_3$ *Pnma*	100 ± 0.9614	5.3117 ± 0.0002	5.5879 ± 0.0003	7.6411 ± 0.0004	1492.36 ± 55.61	10.27 ± 0.0004	1.23	16.81
0.4	YFeO$_3$ *Pnma*	15.97 ± 0.3432	5.3139 ± 0.0010	5.5944 ± 0.0010	7.6461 ± 0.0009	952.63 ± 22.87	7.23 ± 0.0002	1.24	24.59
	Y$_3$Fe$_5$O$_{12}$ *I-a3d*	73.67 ± 0.2156	12.3835 ± 0.0003	-	-	1819.16 ± 126.78	8.68 ± 0.0008		
	Bi$_{25}$FeO$_{40}$ *I-23*	10.36 ± 0.5221	10.0856 ± 0.0014	-	-	999.91 ± 257.04	29.35 ± 0.0003		
0.5	Y$_3$Fe$_5$O$_{12}$ *I-a3d*	86.68 ± 0.3264	12.3931 ± 0.0003	-	-	2768.51 ± 293.71	13.64 ± 0.0004	1.27	25.25
	Bi$_{25}$FeO$_{40}$ *I-23*	13.32 ± 0.5678	10.1573 ± 0.0003	-	-	1625.94 ± 107.13	4.59 ± 0.0001		

Geometrical stability of a perovskite-type phase can be explained by the Goldschmidt tolerance factor (t) [27]. This parameter correlates the symmetry system directly with properties in perovskite-type materials. The tolerance factor value is commonly in the range from 0.80 to 1.10 for perovskites, and especially, for orthorhombic structures which take values in the range of 0.8 to 1 [28]. The Goldschmidt tolerance factor (t) was calculated using the Equation (2) where r_{Bi} and r_Y corresponded to the ionic ratio of Bi^{3+} and Y^{3+} in 6 coordination while r_{Fe} and r_O corresponded to Fe and O ions. The data were obtained from the Shannon ionic radii [26]. The results are presented in Table 2.

$$t = \frac{((1-x)r_Y + x\, r_{Bi}) + r_O}{\sqrt{2}(r_{Fe} + r_O)} \tag{2}$$

In orthorhombic YFeO$_3$ crystal structure, Fe^{3+} ions were surrounded by six O^{2-} which placed an octahedral (FeO$_6$) where O^{2-} ions were located at the corner and shared between two octahedral structures providing two kinds Fe-O-Fe super-exchange bonds. Therefore, there were two bond angles ($\theta 1$ and $\theta 2$ for Fe-O1-Fe and Fe-O2-Fe, respectively). A geometrical relation between $\theta 1$ and $\theta 2$ angles and octahedral tilts (φ_1 and φ_2) were predicted for yttrium orthoferrite using O'Keefe geometrical approximations [29] (Equations (3) and (4)) giving values of angle tilt which is a way to determinate a distortion of the octahedral structure.

$$\theta 1 = \cos^{-1}\left|\frac{2 - 5\cos^2\varphi_1}{2 + \cos^2\varphi_1}\right| \tag{3}$$

$$\theta 2 = \cos^{-1}\left|\frac{1 - 4\cos^2\varphi_2}{3}\right| \tag{4}$$

Table 2. Atomic positions (x, y and z), Fe-O-Fe bond angles ($\theta1$ and $\theta2$), tilt angles (φ_1 and φ_2) and tolerance factor of $YFeO_3$ phase of samples sintered at 700 °C.

Bismuth Content (x)	Elem.	Occ.	Atomic Positions			Bond Angle (Degree)		Tilt Angle (Degree)		
			x	y	z	$\theta1$	$\theta2$	φ_1	φ_2	t (adim)
0	Y	1	0.06399 ± 0.0004	0.2500 ± 0.0000	−0.0174 ± 0.0007	155.16 ± 0.10	142.12 ± 0.80	15.095	23.424	0.834
	Fe	1	0.0000	0.0000	0.5000					
	O1	1	0.4861 ± 0.0026	0.2500 ± 0.0000	0.0779 ± 0.0028					
	O2	1	−0.2975 ± 0.0022	−0.0701 ± 0.0017	0.2986 ± 0.0027					
0.1	Y	0.9	0.0625 ± 0.0005	0.2500 ± 0.0000	−0.0118 ± 0.0010	152.51 ± 0.10	139.29 ± 0.80	16.667	25.215	0.839
	Bi	0.1	0.0625 ± 0.0005	0.2500 ± 0.0000	−0.0118 ± 0.0010					
	Fe	1	0.0000	0.0000	0.5000					
	O1	1	0.4792 ± 0.0035	0.2500 ± 0.0000	0.0852 ± 0.0036					
	O2	1	−0.2967 ± 0.0029	−0.0815 ± 0.0018	0.2951 ± 0.0029					
0.2	Y	0.8	0.0587 ± 0.0004	0.2500 ± 0.0000	−0.0102 ± 0.0007	149.71 ± 0.10	138.54 ± 0.80	18.340	25.691	0.843
	Bi	0.2	0.0587 ± 0.0004	0.2500 ± 0.0000	−0.0102 ± 0.0007					
	Fe	1	0.0000	0.0000	0.5000					
	O1	1	0.4735 ± 0.0024	0.2500 ± 0.0000	0.09329 ± 0.0024					
	O2	1	−0.2983 ± 0.0023	−0.0813 ± 0.0014	0.2973 ± 0.0023					
0.3	Y	0.7	0.0538 ± 0.0004	0.2500 ± 0.0000	−0.0062 ± 0.0007	149.13 ± 0.10	136.63 ± 0.80	18.683	26.907	0.848
	Bi	0.3	0.0538 ± 0.0004	0.2500 ± 0.0000	−0.0062 ± 0.0007					
	Fe	1	0.0000 ± 0.0000	0.0000 ± 0.0000	0.5000 ± 0.0000					
	O1	1	0.4743 ± 0.0025	0.2500 ± 0.0000	0.0955 ± 0.0023					
	O2	1	−0.2935 ± 0.0024	−0.0914 ± 0.0013	0.2881 ± 0.0024					

Magnetic and ferroelectric properties in orthoferrites are strongly dependent of the octahedral tilts of FeO_6, as well as the Fe-O-Fe bond angle, that are important parameters to know. Crystallographic data obtained from Rietveld analysis were represented in Vesta (Visualization for Electronics and Structural Analysis) software [30], in order to determine bond angles $\theta1$ and $\theta2$ of bismuth doped $YFeO_3$ ($Y_{1-x}Bi_xFeO_3$), to calculate the octahedral tilts using Equation (3) and Equation (4). It is important to note that it only can be applied for samples with the orthorhombic crystal structure, that is, samples doped with x equal/lower than 0.3—in this range of doping level, the phase is orthoferrite. The results are presented in Table 2. As can be observed in the calculated data from the XRD patterns, atomic positions of oxygen changed when bismuth content increased. This displacement of oxygen atoms originated a change in two super-exchange bonds angles (i.e., $\theta1$ and $\theta2$) and, consequently, octahedron tilts can be observed from φ_1 and φ_2 angles.

Backscattered electrons micrographs of $Y_{1-x}Bi_xFeO_3$ doped at (a) x = 0, (b) x = 0.3 and (c) x = 0.5 sintered at 700 °C are showed in Figure 2. For sample x = 0 (Figure 2a), it was observed that grain size was approximately ~2 µm. This sample showed two regions with different color tonality associated to materials with different electron density, indicating the presence of two different phases. EDS analysis was carried out on both regions, founding the elements related to phases $YFeO_3$ and

Fe_2O_3 for white grains and small gray grains, respectively. The absence of Fe_2O_3 diffraction peaks in XDR analysis can be explained because their content is under the detection limit of the equipment employed. When x = 0.3 (Figure 2b), larger grain size was observed. This sample showed less porosity and minor porosity size. Also, still present the same phases as an un-doping sample where yttrium orthoferrite (white area) was a majoritarian phase with low quantities of hematite (grey areas). As well as the previous samples, for the sample with x = 0.5 (Figure 2c), only two phases can be observed. Nevertheless, EDS analysis indicated that in this case, the dark-grey regions corresponded to YIG phase and the white one corresponded to sillenite. An increase in grain size was observed in comparison with sample x = 0.3, and the porosity was reduced.
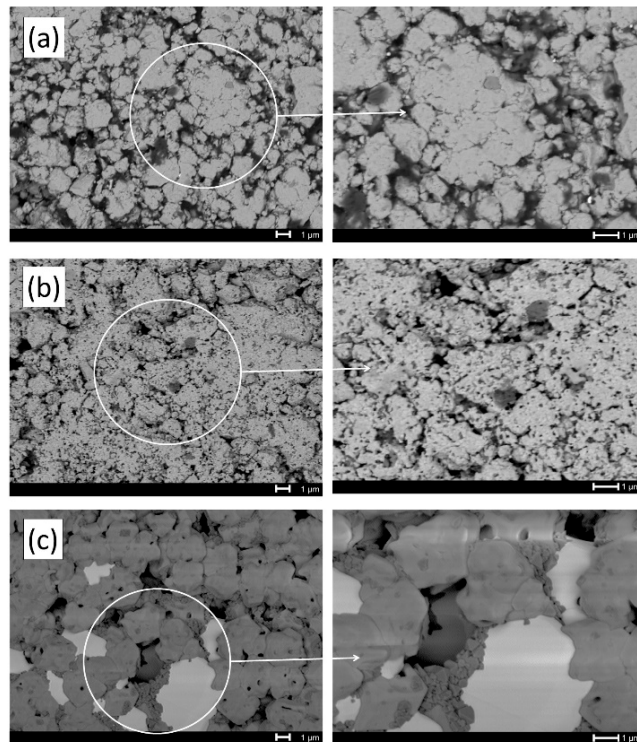
Figure 2. Scanning electron micrographs of samples: (**a**) x = 0, (**b**) x = 0.3 and (**c**) x = 0.5 annealed at 700 °C.

3.2. Magnetic Behavior

Figure 3 shows the magnetic hysteresis loops of the different stoichiometric mixtures of Y_2O_3, Fe_2O_3 and Bi_2O_3 to obtain $Y_{1-x}Bi_xFeO_3$ varying x, from 0 to 0.5. As can be observed, the un-doped $YFeO_3$ (x = 0) mostly showed an antiferromagnetic (AF) G-type order, that is, for each Fe^{3+} with a spin-up, the nearest Fe^{3+} neighbor possessed a spin-down. However, a weak ferromagnetic behavior can be observed for the un-doped sample, which was attributed to the presence of small amounts of Fe_2O_3., It was not detected by XRD analysis (under the limit of detection). Similar AF behavior was observed for samples doped with low Bi^{3+} contents (x ≤ 0.2), concluding that the substitution of Y^{3+} by Bi^{3+} cations did not promote important structural distortions which could modify the magnetic interactions. However, at low bismuth levels, it can be observed that a decrease of the specific magnetization at 18 kOe, with the increase of bismuth content, adscribed to the structure distortion resulting in the modification in Fe-O-Fe bond angle and octahedral tilt [13,20]. For x = 0.3 sample, an interesting modulation of magnetic order by the replacement of the diamagnetic cation Y^{3+} by the diamagnetic Bi^{3+} was observed. It can be correlated with the increase in structure distortion, due to the different ionic radii and tilt angle, together whith the effect of the Dzlayoshinski-Moriya interaction [31],

providing a net magnetic moment. The inset in Figure 3 presented a hysteresis loops magnification for doping concentrations from x = 0 (un-doped) to 0.3.
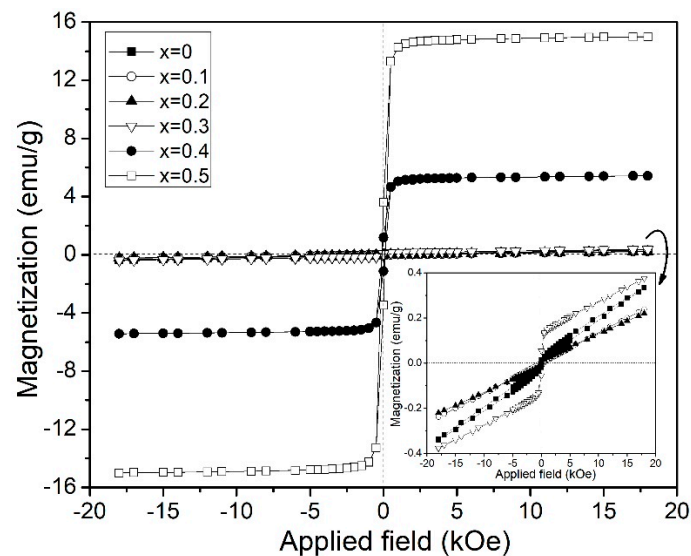
Figure 3. Magnetic hysteresis loops at room temperature of $Y_{1-x}Bi_xFeO_3$ ($0 \leq x \leq 0.5$ $\Delta x = 0.1$) sintered at 700 °C samples. The inset shows a magnification of hysteresis for $0 \leq x \leq 0.3$ samples.

Further, in Figure 3, it was observed that a ferrimagnetic behavior with a low coercive field for x = 0.4, was attributed to the mixed magnetic orders of $Y_3Fe_5O_{12}$, $Bi_{25}FeO_{40}$ and $YFeO_3$. In addition, the increased specific magnetization at 18 kOe for x = 0.5 sample was correlated to the increased amount of the $Y_3Fe_5O_{12}$ phase. In particular, the magnetic order of $Y_3Fe_5O_{12}$ (YIG) prevailed in the magnetic hysteresis loops for x = 0.4 and x = 0.5 samples, due to its phase which was majoritarian in weight percent. However, specific magnetization at 18 kOe was lower as compared to pure $Y_3Fe_5O_{12}$. Lower magnetic values can be explained due to Bi^{3+} cations which were into the $Y_3Fe_5O_{12}$ crystal structure. $Y_3Fe_5O_{12}$ has a cubic crystal structure with eight formula units and three sub-lattices, each one of these three sub-lattices are occupied by Y^{3+}, and two Fe^{3+} cations; for 24c, 16a and 24d sites according to the Wyckoff notation [32,33]. Bi^{3+} cations promoted the formation of a new magnetic sub-lattice, which in turn caused a decrease in the magnetic order. Remanent magnetization slightly varied according to the $Y_3Fe_5O_{12}$ content, from 0.06 to 3.24 emu/g for x = 0.3 and x = 0.5, respectively. However, the magnetic susceptively decreased as the bismuth content increased (from x = 0 to x = 0.3), and adscribed to the crystal distortion. The magnetic parameters obtained from magnetic hysteresis loops are summarized in Table 3.

Table 3. Specific magnetization (M_s), mass magnetic susceptibility (χ_m), remanent magnetization (M_r) and coercive field (H_c) for Bi doped $YFeO_3$.

Bi^{3+} Doping Concentration (x)	M_s at 18 kOe (emu/g)	M_r (emu/g)	H_c (Oe)	χ_m ($\times 10^{-7}$ m^3/kg)
0	0.34	0.02-	710-	2.34
0.1	0.21	-	-	1.66
0.2	0.22	-	-	1.54
0.3	0.38	0.06	495	-
0.4	4.42	1.18	251	-
0.5	14.72	3.24	202	-

Finally, Figure 4 shows the effect of Bi^{3+} in the transition temperatures, Curie (FM to PM) and Néel (AF to PM), for the $Y_{1-x}Bi_xFeO_3$ samples. As can be appreciated, a ferromagnetic to paramagnetic transitions were observed for $0.3 \leq x \leq 0.5$ samples, while an antiferromagnetic to paramagnetic

transitions were observed for $0 \leq x \leq 0.2$ samples. The Néel temperature (Figure 4a) for un-doped samples was approximately 598 K, in good agreement with previous reports for this material [31]. For doped samples, the correlation between the increase of Bi^{3+} concentration and the increase in transition temperatures can be observed, in good agreement with Das et al. [34] and Yuan et al. [20]. This fact is attributed to the modification in the Fe-O-Fe bond angle shown in Table 2. Similar behavior was reported by Treves et al. [35] who proposed a link between average Fe^{3+}-O^{2-}-Fe^{3+} superexchange interaction with magnetic transition temperature, varying the temperature from 740 K to 623 K for $LaFeO_3$ and $LuFeO_3$, respectively.
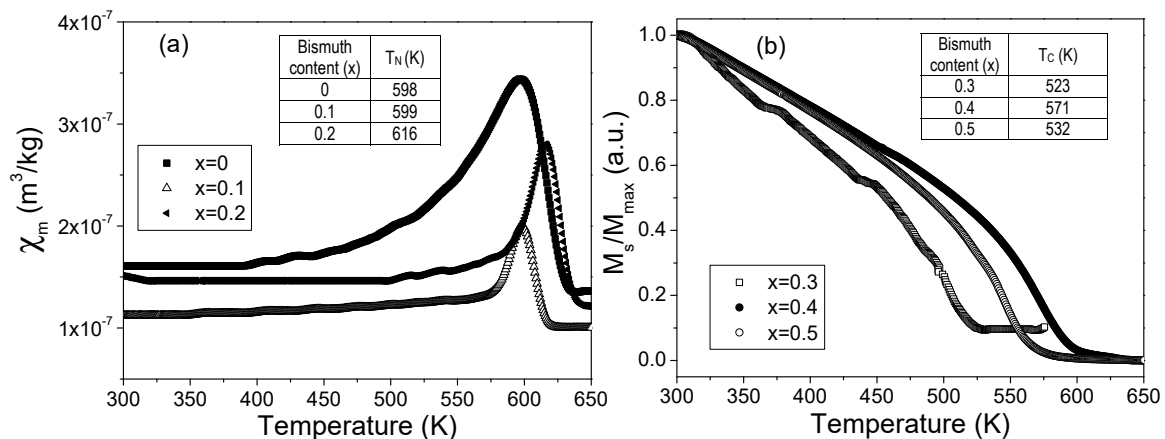
Figure 4. (**a**) Temperature dependence of magnetic susceptibility and, (**b**) magnetization of $Y_{1-x}Bi_xFeO_3$ ($0 \leq x \leq 0.5$, $\Delta x = 0.1$) pressed and sinteredat 700 °C.

$Y_3Fe_5O_{12}$ has a Curie temperature approximately 553K [36], but some authors reported different values, adscribed to the presence of doping cations into the YIG structure, as Baños et al [37], who attributed this modifcation to a new magnetic interaction when Y^{3+} is substituted by Nd^{3+}. The obtained Curie temperatures for x = 0.4 and 0.5 samples were in the range from 520 K to 571 K, around the value for pure $Y_3Fe_5O_{12}$, the variations which have been attributed to the introduction of Bi^{3+} in the crystal structure and, the presence of secondary phases, as observed in the XRD patterns.

3.3. Dielectric Behavior

Impedance spectroscopy was used as an analytical tool to determine dielectric and electric properties of Bi^{3+} doped $YFeO_3$. The frequency response for ferroelectric or dielectric materials usually is expressed in terms of relative complex permittivity (ε_r^*), which is composed for real (ε_r') and imaginary (ε_r'') part, as observed from the relationship $\varepsilon_r^* = \varepsilon_r' - j\varepsilon_r''$ where $j = \sqrt{-1}$. ε' and ε'' are correlated to polarization and energy losses of the system respectively [38]. Both real and imaginary relative permittivity parts can be calculated from impedance spectroscopy with the relation presented in Equations (5) and (6) [3]:

$$\varepsilon_r' = \frac{-Z''}{\omega C_0 (Z'^2 + Z''^2)} \tag{5}$$

$$\varepsilon_r'' = \frac{Z'}{\omega C_0 (Z'^2 + Z''^2)} \tag{6}$$

where ω is angular frequency and C_0 is the geometrical capacitance of the samples. The results of the real part of relative permittivity as a function of frequency are presented in Figure 5. For all samples, values of the real part of relative permittivity were in the range of $\sim 4 \times 10^2$ to $\sim 1 \times 10^2$ and tended to decrease with the increase of frequency. This can be attributed to space charge polarization produced by grain boundaries, and porosity, ascribed to the conformation process, which is in good agreement with the Maxwell-Wagner effect which predicts that at frequencies below 100 kHz, the principal contribution to the relative permittivity are charge accumulators like grain boundaries, defects and

vacancies [39]. When the frequency is above the Maxwell-Wagner effect, it can be proposed that the dipoles responsible of polarization are not able to follow the oscillations of the field, thus an energy dissipation can be produced as evidenced by the reduction in ε_r' values [3,4]. The bismuth doped samples with x = 0.1 and 0.3 presented higher values of ε_r' than the un-doped sample (x = 0), while for x = 0.2 sample, the values were close to the un-doped sample. This increment may be explained by the increase in oxygen vacancies propitiated by Bi^{3+} cation in the samples. Oxygen vacancies are common as an inherent defect produced by heat treatment or doping in perovskite oxide structures [3,40].

This dielectric behaviors are very similar to those in the giant relative permittivity materials such as $Ba(Fe_{1/2}Nb_{1/2})O_3$, $Sr(Fe_{1/2}Nb_{1/2})O_3$, and $Cu_3CaTi_4O_{12}$, however, relative permittivity is several orders lower than the giant relative permittivity materials. The samples with x = 0.4 and x = 0.5 showed a reduction in ε_r' values, in comparison with x = 0.3 sample, that can be correlated to the presence of $Y_3Fe_5O_{12}$ and $Bi_{25}FeO_{40}$ as secondary phases.
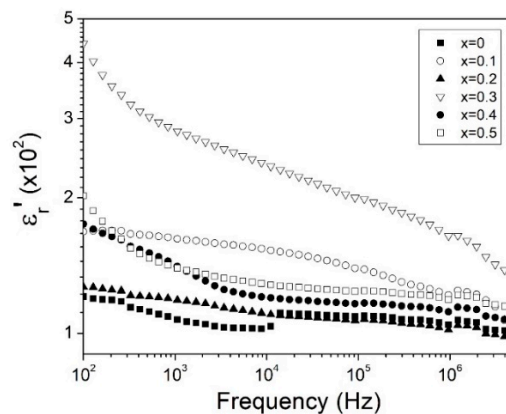
Figure 5. The real part of the complex relative permittivity (ε_r') at room temperature as a function of frequency of Bi^{3+} doped $YFeO_3$ for $0 \leq x \leq 0.5$, $\Delta x = 0.1$, of pressed and sintered samples at 700 °C.

The frequency dependence of the imaginary part of the complex relative permittivity (ε_r'') for doping samples in the ranges of $0 \leq x \leq 0.3$ and $0.4 \leq x \leq 0.5$ are shown in Figure 6a and b, respectively. For all samples ε_r'' showed a clear dependence with the frequency, having values which ranged from 3×10^{-1} to 8×10^{-3} for low and high frequencies respectively. For samples in the range $0 \leq x \leq 0.3$, two regions can be observed; the first region at frequencies lower than 7×10^4 Hz and the second one over the mentioned frequency. These regions are attributed to the two relaxations, as low temperature dielectric relaxation (LTDR) and high temperature dielectric relaxation (HTDR), following Hunpratub nomenclature for $BiFeO_3$ [41], which can be observed at room temperature. On the one hand, the low temperature dielectric relaxation in $YFeO_3$ ceramics originated from the electronic ferroelectricity by taking the possible mixed valence structure Fe^{2+}/Fe^{3+} into account. On the other hand, the high temperature dielectric in $YFeO_3$ ceramics has been related to the point defects, such as oxygen vacancies and the coexistence of Fe^{2+} and Fe^{3+}, which have been generally formed during sintering in air. In the same way for samples in $0 \leq x \leq 0.3$ range, the relaxation observed in the second region was more evident when bismuth concentration was increasing.

For samples with Bi^{3+} doping concentrations above 0.4, three zones can be recognized for ε_r'', the first (I) at frequencies lower than 4×10^4 Hz, the second (II) from 4×10^4 to 1×10^6 Hz, and the last one (III), at frequencies from 1×10^6 to 5×10^6 Hz. Each of these zones corresponded to a relaxation process. These relaxations showed an increase in comparison with samples with lower bismuth which may be attributed to the presence of secondary phases, especially bismuth. As can be observed, the bismuth concentration directly correlated to changes in the relaxation process in all samples. It has been demonstrated that doping produces the appearance of new dielectric relaxation that can be associated at oxygen vacancies [11,17]. Liberated electrons from oxygen vacancies can be taken by Fe^{3+} ions and change their oxidation state to Fe^{2+} ions [42]. The hopping of the electrons through the

Fe^{2+}-O^{2-}-Fe^{3+} bond chains, which is equivalent to the dipole reorientation under ac fields, can also give rise to the dielectric relaxation in $Y_{1-x}Bi_xFeO_3$ samples.
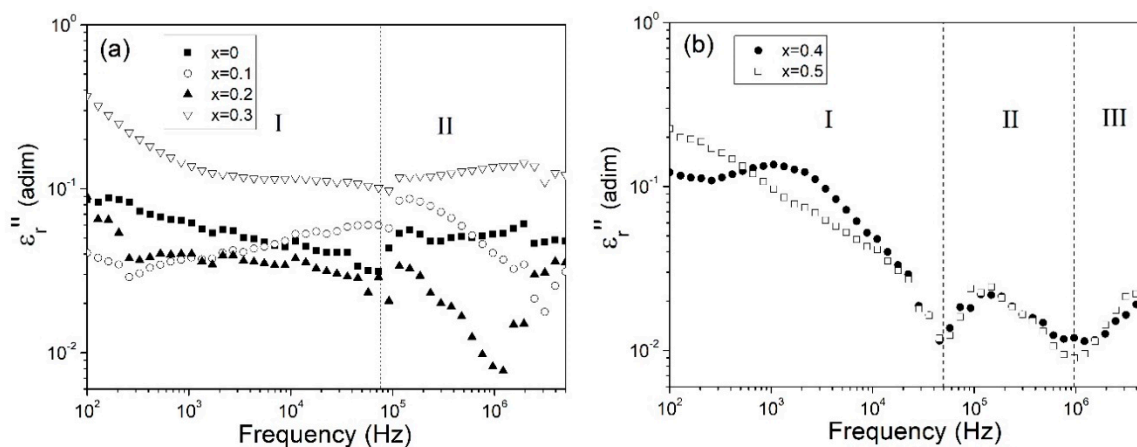
Figure 6. The imaginary part of the complex relative permittivity (ε'') at room temperature as function of frequency of $Y_{1-x}Bi_xFeO_3$ in the range of (**a**) $0 \leq x \leq 0.3$ and (**b**) $0.4 \leq x \leq 0.5$, of pressed and sintered samples at 700 °C.

3.4. Conductivity and Leakage Current

In order to determine the effect of alternating current conductivity (σ_{ac}) in dielectric properties at room temperature of selected samples, σ_{ac} was calculated employing the relation shown in Equation (7):

$$\sigma_{ac} = \frac{Z'}{Z'^2 + Z''^2}\frac{d}{A} \tag{7}$$

where Z' and Z'' correspond to the real and imaginary part of complex impedance, A is the cross-sectional area and d is the thickness of the sample. Frequency dependence of σ_{ac} is presented in Figure 7. For all doping concentrations, the σ_{ac} increased as the frequency was augmented. The increased conductivity can be attributed to the transition from electronic to ionic conduction [39]. Similar behavior has been reported for other ferrites, where grain boundaries acted like insulators between grains reducing electron mobility [43,44]. The increased frequency reduced the effect of grain boundaries, which increased the conductivity. Also, the conductivity increased when the bismuth doping concentration increased. This behavior can be attributed to an increase in oxygen vacancies, besides the grain size. Oxygen vacancies can be produced in many ways as sintering at high temperatures or, destabilization in the structure. Changes in the crystal structure, especially referred to the Fe-O bond, produced oxygen vacancies which caused an increase in Fe^{2+} and in consequence, an increase in hopping charge carriers and conductivity [45]. Additionally to oxygen vacancies, increased grains size propitiated a reduction of grain boundaries in the doped samples, and then reduced physical barriers that inhibited electron mobility, which increased the conductivity. Finally, as can be seen in Figure 7, the alternating current conductivity (σ_{ac}), for all evaluated samples, were in the range of the semiconductor materials from ~1×10^{-6} to ~4×10^{-1} S/cm, for 10^2 and 5×10^6 Hz, respectively.
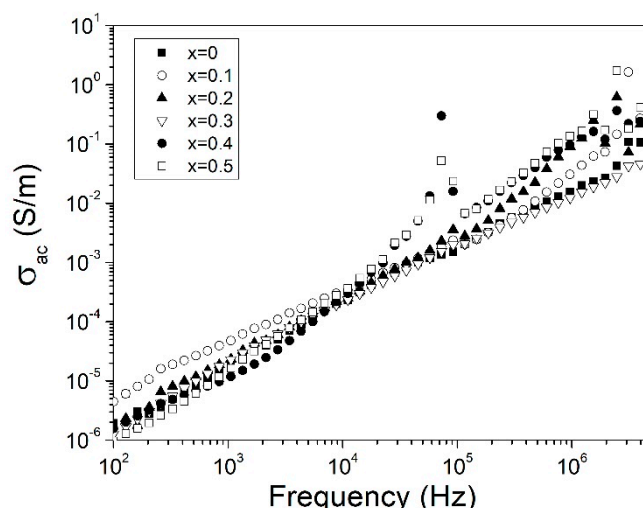
Figure 7. Alternating current conductivity (σ_{AC}) at room temperature of $Y_{1-x}Bi_xFeO_3$ varying *x* from 0 to 0.5, of pellets sintered at 700 °C.

Leakage current dependence as a function of applied voltage of positive bias was measured for the selected samples. Figure 8 presents the leakage current density (J) versus electric field (E) for Bi^{3+} doped samples at different concentrations, $0 \leq x \leq 0.5$. For all the samples, the behavior of current density showed a very sharp slope at low field values followed by a less steep slope, which was not able to reach saturation due to the limitation of the applied field from the LCR meter. The leakage current in ceramics samples has been affected by factors as microstructure, vacancy oxygen, and grain size and their boundaries as they provided conduction pathways [46,47]. Lubomirsky found that contact produced by the contact between grains of very different sizes lead to exchanging between them, known as heterosize charging [48]. Reddy et al. reported that leakage current was affected by non-uniform grain structures and porous structures, which were the product of heterosize charging [49]. Bismuth doping reduced the leakage current, in comparison with the un-doped sample, which showed the lowest value for x = 0.1. The leakage current reduction can be correlated to increased crystallinity and reduced porosity as has been observed previously in XRD and SEM respectively. As can be observed from the SEM micrographs, Bi^{3+} reduced porosity and increased grain size providing a more homogeneous structure which reduced the leakage current by a reduction in heterosize charging. Hasan et al. and Das et al. have reported that the substitution of a smaller cation for a larger one produced a reduction in movable charge density and reduced the leakage current [7,34]. Similar behavior may have occurred when the Y^{3+} cation was substituted for a larger Bi^{3+} cation, which reduced movable charges in comparison with the un-doped sample. In addition, the increased leakage current density when bismuth contained > 0.3 may be attributed to the coexistence of multiple phases which produced an increment of heterosize charging due to the coexistence of different grains morphologies and grain boundaries.
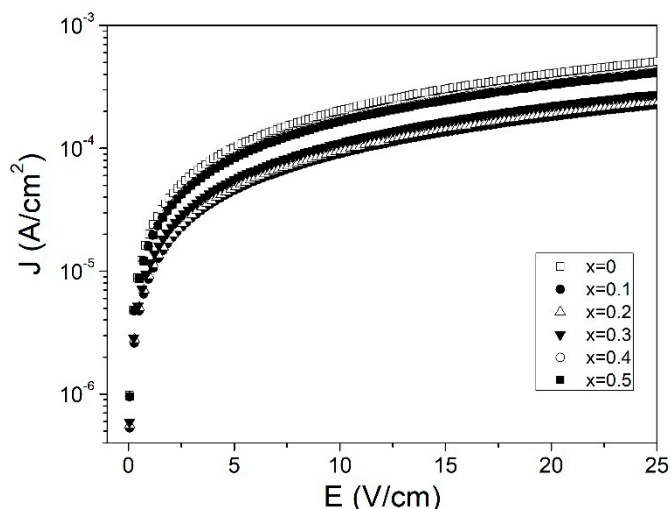
Figure 8. The leakage current density as function of electric field at room temperature of $Y_{1-x}Bi_xFeO_3$ with $0 \leq x \leq 0.5$ samples sintered at 700 °C.

4. Conclusions

Ceramic samples $Y_{1-x}Bi_xFeO_3$ at doping concentrations $0 \leq x \leq 0.5$, were synthesized by means of high-energy ball milling followed by pressing and sintered at 700 °C. Their magnetic and dielectric properties were evaluated. The Bi^{3+} doping concentrations, below $x = 0.3$, affected the lattice parameters but did not produce crystal structure transitions, keeping the orthorhombic structure of yttrium orthoferrite. An increase in the octahedral angle tilt was observed when the addition of Bi^{3+} was increased, providing a path for change for both magnetic and dielectric behavior. A weak magnetic moment was found for sample with $x = 0.3$ which was attributed to both the crystal distortion and the Dzyaloshinskii-Moriya interaction. For doping concentrations of Bi^{3+} higher than $x = 0.3$, crystal structure transformations were produced from yttrium orthoferrite to $Y_3Fe_5O_{12}$ and $Bi_{25}FeO_{40}$. The samples mainly composed with YIG possessed a significant ferromagnetic order, but with saturation magnetization, the amount lowered due to the paramagnetic contribution of sillenite as a secondary phase. The dielectric behavior presented great similitude with the giant dielectric constant material. However, the magnitude order was lower than these materials. In order to understand this phenomenon, it is necessary to undertake an investigation in relation to temperature and dielectric behavior. The Bi^{3+} and sintering process promoted the formation of oxygen vacancies and increased conductivity. The Bi^{3+} reduced the leakage current of yttrium orthoferrite due to an increase in grain, crystallite size and a reduction in porosity.

References

1. Spaldin, N.A. Multiferroics: Past, present, and future. *MRS Bull.* **2017**, *42*, 385–390. [CrossRef]
2. Chen, F.; Zhang, Z.; Wang, X.; Ouyang, J.; Feng, Z.; Su, Z.; Chen, Y.; Harris, V.G. Room temperature magnetoelectric effect of YFeO$_3$ –Y$_3$Fe$_5$O$_{12}$ ferrite composites. *J. Alloy. Compd.* **2016**, *656*, 465–469. [CrossRef]

3.　Deka, B.; Ravi, S.; Perumal, A.; Pamu, D. Effect of Mn doping on magnetic and dielectric properties of $YFeO_3$. *Ceram. Int.* **2017**, *43*, 1323–1334. [CrossRef]

4.　Stoeffler, D.; Chaker, Z. First principles study of the electronic structure and magnetic properties of $YFeO_3$ oxide. *J. Magn. Magn. Mater.* **2017**, *442*, 255–264. [CrossRef]

5.　Zhang, M.; Yasui, S.; Katayama, T.; Rao, B.N.; Wen, H.; Pan, X.; Tang, M.; Ai, F.; Itoh, M. Epitaxial Growth of Orthorhombic $GaFeO_3$ Thin Films on $SrTiO_3$ (111) Substrates by Simple Sol-Gel Method. *Materials* **2019**, *12*, 254. [CrossRef] [PubMed]

6.　Pedro-García, F.; Sánchez-De Jesús, F.; Cortés-Escobedo, C.; Barba-Pingarrón, A.; Bolarín-Miró, A. Mechanically assisted synthesis of multiferroic $BiFeO_3$: Effect of synthesis parameters. *J. Alloy. Compd.* **2017**, *711*, 77–84. [CrossRef]

7.　Hasan, M.; Hakim, M.A.; Basith, M.A.; Hossain, M.S.; Ahmmad, B.; Zubair, M.A.; Hussain, A.; Islam, M.F. Size dependent magnetic and electrical properties of Ba-doped nanocrystalline $BiFeO_3$. *AIP Adv.* **2016**, *6*, 35314. [CrossRef]

8.　Kao, M.C.; Chen, H.Z.; Young, S.L.; Chen, K.H.; Chiang, J.L.; Shi, J. Bin Structural, electrical, magnetic and resistive switching properties of the Multiferroic/Ferroelectric bilayer thin films. *Materials* **2017**, *10*, 1327. [CrossRef]

9.　Pedro-García, F.; Bolarín-Miró, A.M.; Sánchez-De Jesús, F.; Cortés-Escobedo, C.A.; Valdez-Nava, Z.; Torres-Villaseñor, G. Stabilization of α-$BiFeO_3$ structure by Sr^{2+} and its effect on multiferroic properties. *Ceram. Int.* **2018**, *44*, 8087–8093. [CrossRef]

10.　Wang, M.; Wang, T.; Song, S.-H.; Ravi, M.; Liu, R.-C.; Ji, S.-S. Effect of calcination temperature on structural, magnetic and optical properties of multiferroic $YFeO_3$ nanopowders synthesized by a low temperature solid-state reaction. *Ceram. Int.* **2017**, *43*, 10270–10276. [CrossRef]

11.　Madolappa, S.; Ponraj, B.; Bhimireddi, R.; Varma, K.B.R. Enhanced magnetic and dielectric properties of Ti-doped $YFeO_3$ ceramics. *J. Am. Ceram. Soc.* **2017**, *100*, 2641–2650. [CrossRef]

12.　Wang, M.; Wang, T.; Song, S.; Tan, M. Structure-Controllable Synthesis of Multiferroic $YFeO_3$ Nanopowders and Their Optical and Magnetic Properties. *Materials* **2017**, *10*, 626. [CrossRef] [PubMed]

13.　Song, H.; Jiang, G. Effects of Nd, Er Doping on the Structure and Magnetic Properties of $YFeO_3$. *J. Supercond. Nov. Magn.* **2017**, *31*, 2511–2517. [CrossRef]

14.　Tan, Q.; Wang, Q.; Liu, Y. Magnetic Properties and Spontaneous Polarization of La-, Mn- and N-Doped Tetragonal $BiFeO_3$: A First-Principles Study. *Materials* **2018**, *11*, 985. [CrossRef] [PubMed]

15.　Shang, M.; Zhang, C.; Zhang, T.; Yuan, L.; Ge, L. The multiferroic perovskite $YFeO_3$. *Appl. Phys. Lett.* **2013**, *102*, 062903. [CrossRef]

16.　Chowdhury, U.; Goswami, S.; Bhattacharya, D.; Ghosh, J.; Basu, S.; Neogi, S. Room temperature multiferroicity in orthorhombic $LuFeO_3$. *Appl. Phys. Lett.* **2014**, *105*, 052911. [CrossRef]

17.　Zhang, C.; Wang, X.; Wang, Z.; Yan, H.; Li, H.; Li, L. Dielectric relaxation, electric modulus and ac conductivity of Mn-doped $YFeO_3$. *Ceram. Int.* **2016**, *42*, 19461–19465. [CrossRef]

18.　Das, I.; Chanda, S.; Dutta, A.; Banerjee, S.; Sinha, T. Dielectric relaxation of $Y_{1-x}R_xFeO_3$ (R=Dy, Er, x=0, 0.5). *J. Alloy. Compd.* **2013**, *571*, 56–62. [CrossRef]

19.　Jacob, K.T.; Rajitha, G.; Dasgupta, N. Electrical conductivity of Ca-doped $YFeO_3$. *Indian J. Eng. Mater. Sci.* **2012**, *19*, 47–53.

20.　Yuan, X.; Sun, Y.; Xu, M. Effect of Gd substitution on the structure and magnetic properties of $YFeO_3$ ceramics. *J. Solid State Chem.* **2012**, *196*, 362–366. [CrossRef]

21.　Bolarín-Miró, A.; Sánchez-De Jesús, F.; Cortés-Escobedo, C.; Valenzuela, R.; Ammar, S. Structure and magnetic properties of $Gd_xY_{1-x}FeO_3$ obtained by mechanosynthesis. *J. Alloy. Compd.* **2014**, *586*, S90–S94. [CrossRef]

22.　Cheng, M.; Jiang, G.; Yang, W.; Duan, L.; Peng, W.; Chen, J.; Wang, X. Study of Y1-xErxFeO3 (0<x<1) powder synthesized by sol–gel method and their magnetic properties. *J. Magn. Magn. Mater.* **2016**, *417*, 87–91.

23.　Lutterotti, L.; Matthies, S.; Wenk, H.-R.; Schultz, A.S.; Richardson, J.W. Combined texture and structure analysis of deformed limestone from time-of-flight neutron diffraction spectra. *J. Appl. Phys.* **1997**, *81*, 594–600. [CrossRef]

24.　Van Hook, H.J. Phase Relations in the System Fe_2O_3-Fe_3O_4-$YFeO_3$ in Air. *J. Am. Ceram. Soc.* **1961**, *44*, 208–214. [CrossRef]

25.　Van Hook, H.J. Phase Relations in the Ternary System Fe_2O_3-FeO-$YFeO_3$. *J. Am. Ceram. Soc.* **1962**, *45*, 162–165. [CrossRef]

26. Shannon, R.D. Revised effective ionic radii and systematic studies of interatomic distances in halides and chalcogenides. *Acta Crystallogr. Sect. A Cryst. Phys. Diffr. Theor. Gen. Crystallogr.* **1976**, *32*, 751–767. [CrossRef]

27. Moure, C.; Pena, O. Recent advances in perovskites: Processing and properties. *Prog. Solid State Chem.* **2015**, *43*, 123–148. [CrossRef]

28. Nagashio, K.; Kuribayashi, K. Metastable Phase Formation from an Undercooled Rare-Earth Orthoferrite Melt. *J. Am. Ceram. Soc.* **2002**, *85*, 2550–2556. [CrossRef]

29. O'Keeffe, M.; Hyde, B.G. Some structures topologically related to cubic perovskite ($E2_1$), ReO_3 ($D0_9$) and Cu_3Au ($L1_2$). *Acta Crystallogr. Sect. B Struct. Crystallogr. Cryst. Chem.* **1977**, *33*, 3802–3813. [CrossRef]

30. Momma, K.; Izumi, F. VESTA 3 for three-dimensional visualization of crystal, volumetric and morphology data. *J. Appl. Crystallogr.* **2011**, *44*, 1272–1276. [CrossRef]

31. Rosales-González, O.; Jesús, F.S.-D.; Cortés-Escobedo, C.; Bolarín-Miró, A. Crystal structure and multiferroic behavior of perovskite $YFeO_3$. *Ceram. Int.* **2018**, *44*, 15298–15303. [CrossRef]

32. Baños-López, E.; Cortés-Escobedo, C.; Jesús, F.S.-D.; Barba-Pingarrón, A.; Bolarín-Miró, A. Crystal structure and magnetic properties of cerium-doped YIG: Effect of doping concentration and annealing temperature. *J. Alloy. Compd.* **2018**, *730*, 127–134. [CrossRef]

33. Anupama, A.; Kumar, R.; Choudhary, H.K.; Sahoo, B. Synthesis of coral-shaped yttrium-aluminium-iron garnets by solution-combustion method. *Ceram. Int.* **2018**, *44*, 3024–3031. [CrossRef]

34. Das, R.; Mandal, K. Magnetic, ferroelectric and magnetoelectric properties of Ba-doped $BiFeO_3$. *J. Magn. Magn. Mater.* **2012**, *324*, 1913–1918. [CrossRef]

35. Treves, D.; Eibschütz, M.; Coppens, P. Dependence of superexchange interaction on Fe^{3+}-O^{2-}-Fe^{3+} linkage angle. *Phys. Lett.* **1965**, *18*, 216–217. [CrossRef]

36. Mallmann, E.J.J.; Sombra, A.S.B.; Goes, J.C.; Fechine, P.B.A. Yttrium Iron Garnet: Properties and Applications Review. *Solid State Phenom.* **2013**, *202*, 65–96. [CrossRef]

37. Baños, E.; Sánchez-De Jesús, F.; Cortés, C.A.; Bolarin-Miró, A.M. Enhancement in Curie Temperature of Yttrium Iron Garnet by Doping with Neodymium. *Materials* **2018**, *11*, 1652.

38. Elissalde, C.; Ravez, J. Ferroelectric ceramics: defects and dielectric relaxations. *J. Mater. Chem.* **2001**, *11*, 1957–1967. [CrossRef]

39. Betancourt-Cantera, L.; Bolarín-Miró, A.M.; Cortés-Escobedo, C.; Hernández-Cruz, L.; Sánchez-De Jesús, F. Structural transitions and multiferroic properties of high Ni-doped $BiFeO_3$. *J. Magn. Magn. Mater.* **2018**, *456*, 381–389. [CrossRef]

40. Jabbarzare, S.; Abdellahi, M.; Ghayour, H.; Chami, A.; Hejazian, S. Mechanochemically assisted synthesis of yttrium ferrite ceramic and its visible light photocatalytic and magnetic properties. *J. Alloy. Compd.* **2016**, *688*, 1125–1130. [CrossRef]

41. Hunpratub, S.; Thongbai, P.; Yamwong, T.; Yimnirun, R.; Maensiri, S. Dielectric relaxations and dielectric response in multiferroic $BiFeO_3$ ceramics. *Appl. Phys. Lett.* **2009**, *94*, 062904. [CrossRef]

42. Raut, S.; Babu, P.D.; Sharma, R.K.; Pattanayak, R.; Panigrahi, S. Grain boundary-dominated electrical conduction and anomalous optical-phonon behaviour near the Neel temperature in $YFeO_3$ ceramics. *J. Appl. Phys.* **2018**, *123*, 174101. [CrossRef]

43. Ahmad, T.; Lone, I.H.; Ansari, S.; Ahmed, J.; Ahamad, T.; AlShehri, S.M. Multifunctional properties and applications of yttrium ferrite nanoparticles prepared by citrate precursor route. *Mater. Des.* **2017**, *126*, 331–338. [CrossRef]

44. Zahi, S.; Daud, A.; Hashim, M. A comparative study of nickel–zinc ferrites by sol–gel route and solid-state reaction. *Mater. Chem. Phys.* **2007**, *106*, 452–456. [CrossRef]

45. Aakansha; Deka, B.; Ravi, S.; Pamu, D. Impedance spectroscopy and ac conductivity mechanism in Sm doped Yttrium Iron Garnet. *Ceram. Int.* **2017**, *43*, 10468–10477. [CrossRef]

46. Hussain, S.; Hasanain, S.; Jaffari, G.H.; Shah, S.I. Thickness dependent magnetic and ferroelectric properties of $LaNiO_3$ buffered $BiFeO_3$ thin films. *Curr. Appl. Phys.* **2015**, *15*, 194–200. [CrossRef]

47. Reddy, V.R.; Kothari, D.; Upadhyay, S.K.; Gupta, A.; Chauhan, N.; Awasthi, A. Reduced leakage current of multiferroic $BiFeO_3$ ceramics with microwave synthesis. *Ceram. Int.* **2014**, *40*, 4247–4250. [CrossRef]

48. Lubomirsky, I.; Fleig, J.; Maier, J. Modeling of space-charge effects in nanocrystalline ceramics: The influence of geometry. *J. Appl. Phys.* **2007**, *92*, 6819. [CrossRef]

49. Reddy, S.S.K.; Raju, N.; Reddy, C.G.; Reddy, P.Y.; Reddy, K.R.; Gupta, S.; Reddy, V.R. Study of Mn doped multiferroic DyFeO$_3$ ceramics. *Ceram. Int.* **2017**, *43*, 6148–6155. [CrossRef]